Supporting Information

For

Hyperbranched Phosphorus Flame Retardants: Multifunctional Additives for Epoxy Resins

Alexander Battig,[a‡] Jens C. Markwart,[b,c‡] Frederik R. Wurm,[b] and Bernhard Schartel[a*]

[a] Bundesanstalt für Materialforschung und -prüfung (BAM), Unter den Eichen 87, 12205 Berlin, Germany.
[b] Max Planck Institute for Polymer Research, Ackermannweg 10, 55128 Mainz, Germany.
[c] Graduate School Materials Science in Mainz, Staudinger Weg 9, 55128 Mainz, Germany.

Structure Characterization: ^{1}H and ^{31}P NMR

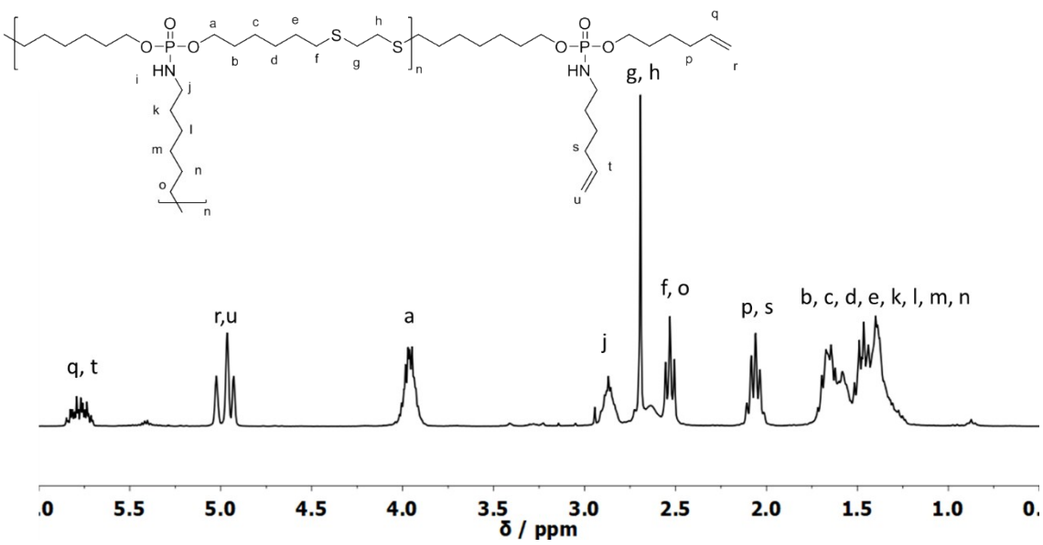

Figure S1. ^{1}H NMR (300 MHz in $CDCl_3$ at 298 K) of *hb*-polyphosphoramidate (**3**).

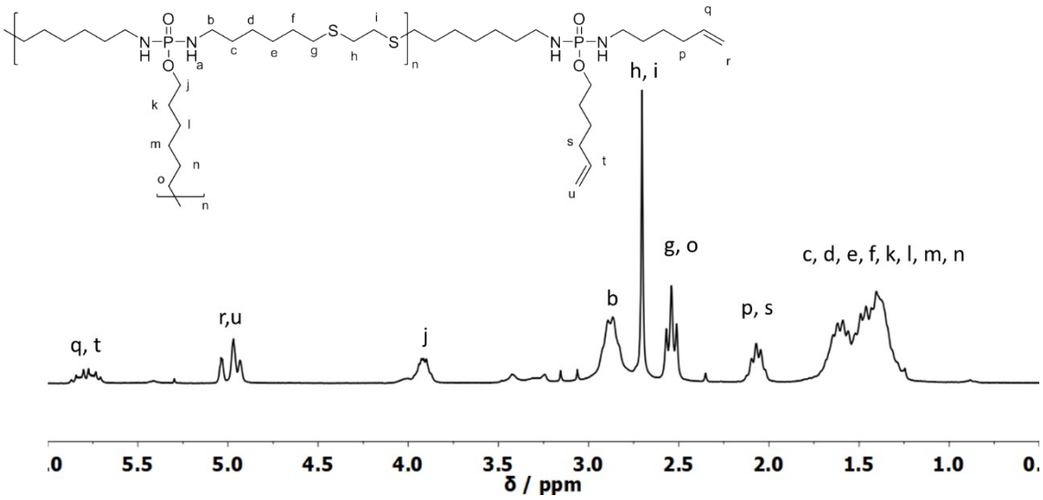

Figure S2. ^{1}H NMR (300 MHz in $CDCl_3$ at 298 K) of *hb*-polyphosphorodiamidate (**2**).

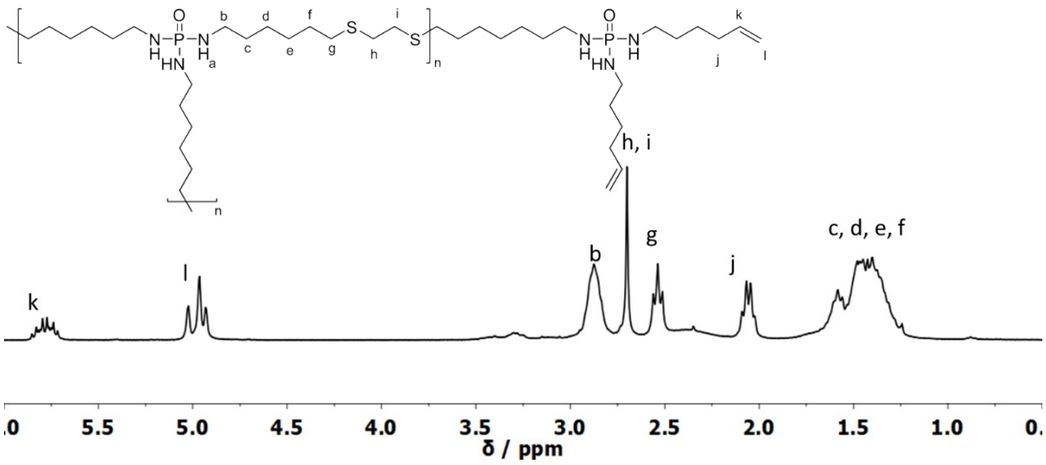

Figure S3. ^{1}H NMR (300 MHz in $CDCl_3$ at 298 K) of *hb*-polyphosphoramide (**1**).

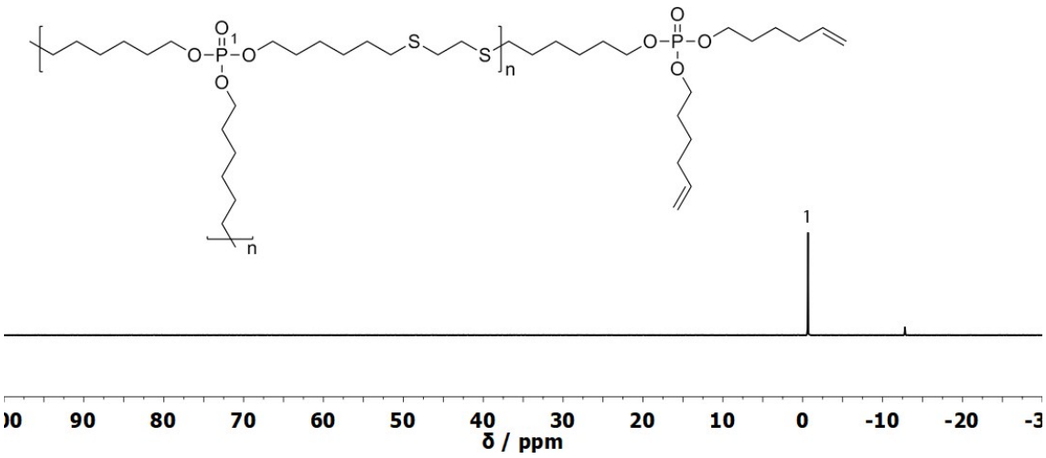

Figure S4. ^{31}P {H} NMR (121 MHz in $CDCl_3$ at 298 K) of *hb*-polyphosphate (**4**).

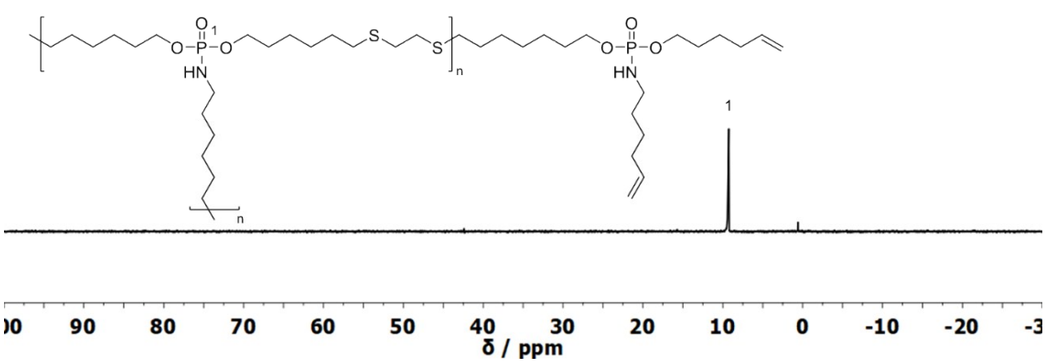

Figure S5. ^{31}P {H} NMR (121 MHz in $CDCl_3$ at 298 K) of *hb*-polyphosphoramidate (**3**).

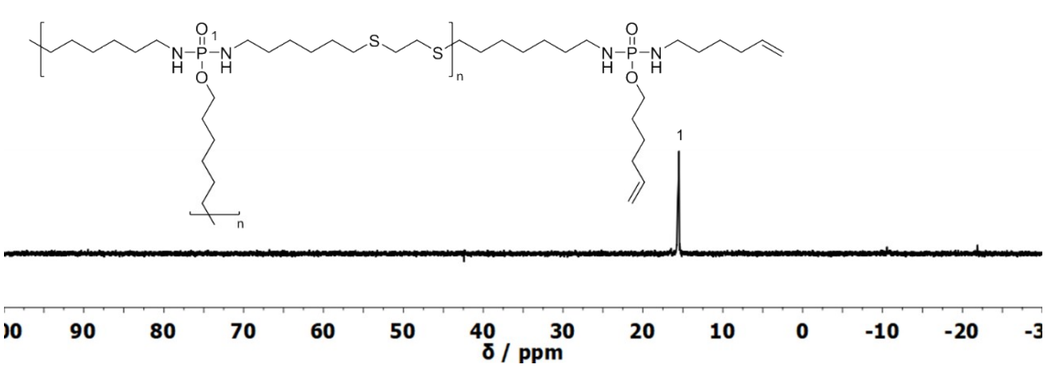

Figure S6. ^{31}P {H} NMR (121 MHz in $CDCl_3$ at 298 K) of *hb*-polyphosphorodiamidate (**2**).

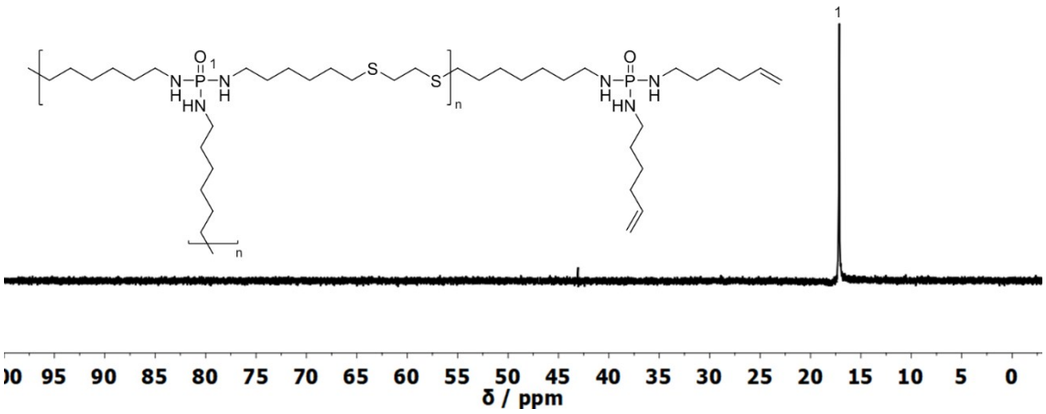

Figure S7. ^{31}P {H} NMR (121 MHz in $CDCl_3$ at 298 K) of *hb*-polyphosphoramide (**1**).

Polymerization study

Table S1. Variation of polymerization conditions at different A_2:B_3 ratios. A_2 is 1,2-ethanedithiol and B_3 is tri(hex-5-en-1-yl)phosphate.

Ratio*	CL	time until CL / min	M_n / g mol^{-1}	M_w / g mol^{-1}	PDI	Yield / %
10:5	Yes	180	-	-	-	-
5:6	Yes	24	-	-	-	-
5:7	Yes	103	-	-	-	-
5:8	Yes	120	-	-	-	-
5:9	No	-	4,300	53,400	12.44	87
5:10	No	-	3,400	11,300	3.29	82
5:11	No	-	3,000	7,900	2.66	79

* molar feed ratio of functional groups, i.e. thiols : double bonds.

Material Properties: Differential Scanning Calorimetry

Table S2. Glass-transition temperatures (T_g) of *hb*-FRs determined *via* differential scanning calorimetry (DSC).

	hb phosphate (**4**)	*hb* amidate (**3**)	*hb* diamidate (**2**)	*hb* amide (**1**)
T_g / °C	-94	-81	-62	-48

Pyrolysis: Thermogravimetric Analysis of *hb*-FRs

Table S3. Results from thermogravimetric analysis (TGA) of *hb*-FRs under pyrolytic conditions (N_2 flow = 30 ml min^{-1}, heating rate = 10 K min^{-1}).

Material	hb Phosphate (**4**)	hb Amidate (**3**)	hb Diamidate (**2**)	hb Amide (**1**)
$T_{5\%}$ / °C	241 ± 2	245 ± 3	194 ± 5	190 ± 3
T_1 / °C [preceeding main decomposition step]	-	-	257 ± 5	273 ± 3
T_{max} / °C [main decomposition step]	274 ± 3	281 ± 0	359 ± 2	361 ± 4
T_2 / °C [1st subsequent decomposition step]	-	335 ± 4	-	-
T_3 / °C [2nd subsequent decomposition step]	-	481 ± 0	461 ±3	428 ± 3
Residue / wt.-% (at 700 °C)	11 ± 1	12 ± 0	14 ± 1	18 ± 0

Proposed decomposition mechanisms: Hydrolysis

Scheme S1. Proposed decomposition mechanism of hydrolysis reactions during pyrolysis.

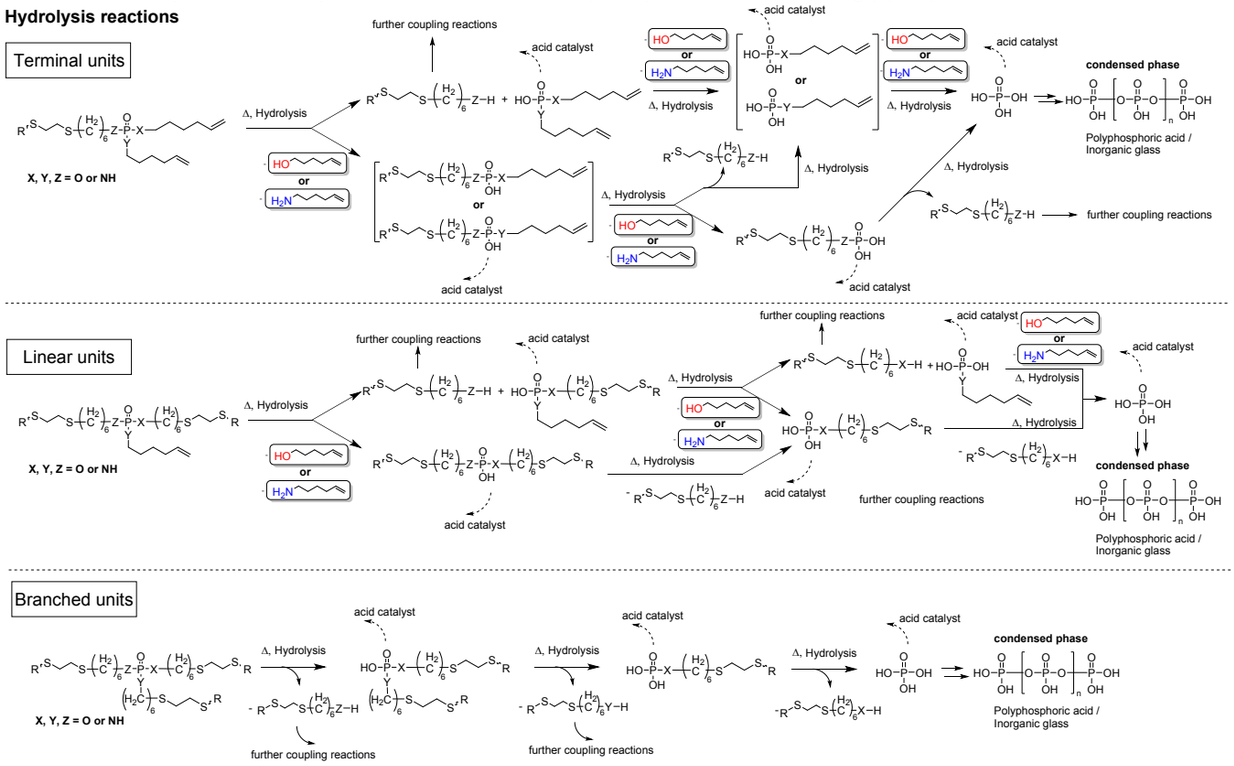

Hydrolysis reactions of phosphates/-amides (Scheme S2) produce phosphates that act as acid catalysts, thereby promoting further hydrolysis reactions.[1] For terminal units and linear units in our P-FRs, two hydrolysis pathways could occur: either the P-(O-C_6H_{11}) or P-(NH-C_6H_{11}) bond can be hydrolyzed, leading to the production of 5-hexene-1-ol or 5-hexene-1-amine, respectively (side chain reaction in linear and terminal units), or alternatively, the P-(O-R) or P-(NH-R) bond connecting the unit to the polymer backbone is hydrolyzed (main chain reaction). Main chain reactions yield new functional groups which could undergo further coupling reactions, e.g. transesterification.[2] Sufficient hydrolysis reactions lead to the cleavage of the phosphorus-containing moiety from the main chain. Complete hydrolysis leads to the formation of phosphoric acid,[3] which typically polymerizes under these conditions to polyphosphoric acid or inorganic glasses in the condensed phase.[4]

Proposed decomposition mechanisms: *cis*-Elimination

Scheme S2. Proposed decomposition mechanism of elimination reactions during pyrolysis.

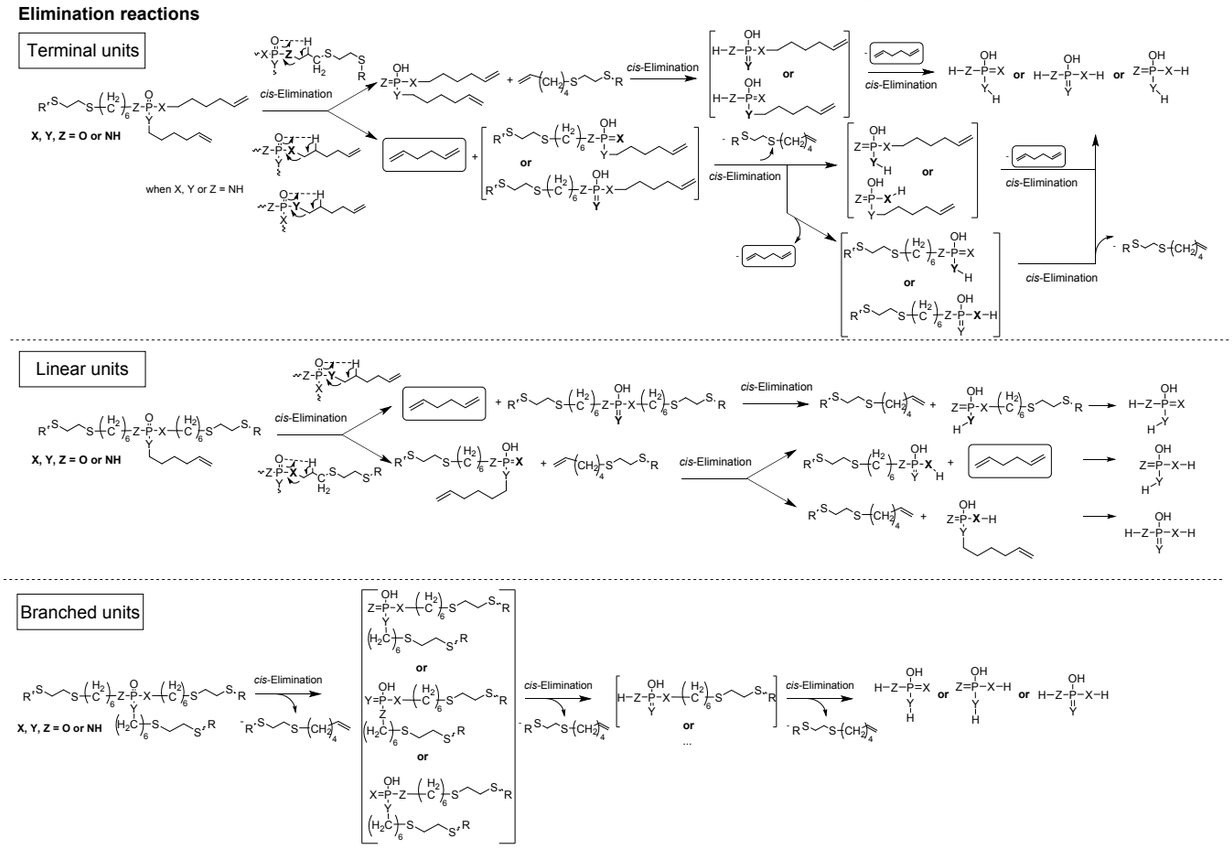

Besides hydrolysis, elimination reactions (Scheme S3) involve the hydrogen atom in the *cis*-position (relative to the P=O bond) of the β-CH_2 moiety of the hydrocarbon chain.[5-7] Here, hydrogen bonding facilitates the cleavage of the (O-C) or (N-C) bond, generating either 1,5-hexadiene (side chain reaction) or a terminal allyl group (main chain reaction), the latter forming new vinyl groups that undergo cross-linking reactions during decomposition, e.g. *via* radical initiation or cyclization. For N-containing *hb*-FRs, elimination reactions could produce P=N bond, which could further lead to the formation of phosphazenes, phosphorus oxynitrides, or other $(P\text{-}O\text{-}N)_x$ compounds in the condensed phase through rearrangement and polymerization processes during thermal decomposition.[8, 9]

Proposed decomposition mechanisms: Inter-/intramolecular reactions

Scheme S3. Proposed decomposition mechanism of inter- and intramolecular reactions during pyrolysis.

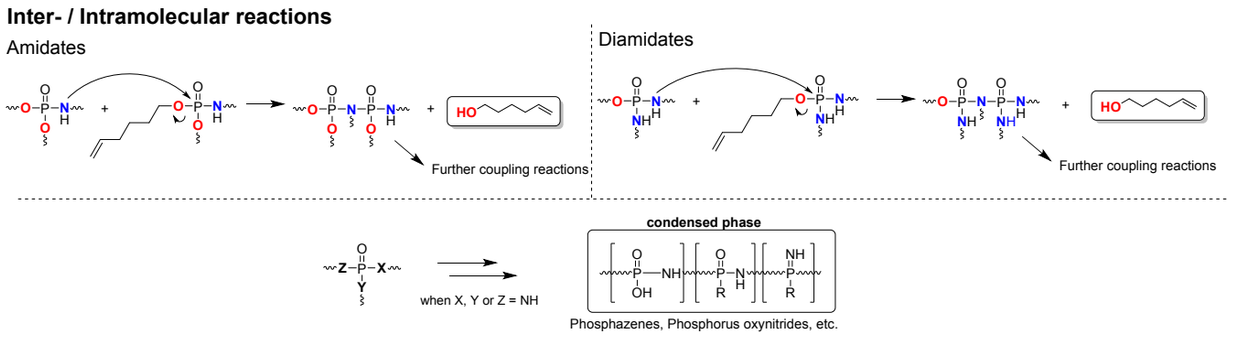

Additionally, inter- and intramolecular reactions (Scheme S4) can occur between two separate molecules, two moieties of the same hyperbranched polymer, or between the FR and matrix. These reactions occur in nitrogen-containing compounds like phosphoramidates, -diamidates, and amides. While the secondary amine acts as a base, the amine hydrogen attacks the pentavalent P of a P-N bond in the vicinity.[10] As a result, 5-hexene-1-ol is produced in an addition-elimination-type reaction. For nitrogen-containing compounds, inter- and intramolecular reactions, as well as rearrangements, may also lead to the formation of thermally stable phosphazenes, phosphorus-oxynitrides, and other $(P\text{-}O\text{-}N)_x$ species.[11, 12]

Proposed decomposition mechanisms: Sulfur components

Scheme S4. Proposed decomposition mechanism leading to the formation of cyclic sulfur-components

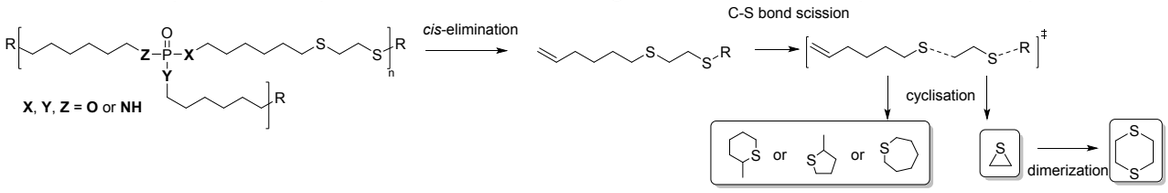

The scission of C-S-bonds of *cis*-elimination products (see Scheme S2) could lead to $C_6H_{12}S$ and C_2H_4S fragments. Cyclisation of the former leads to 4-methylthiane, 2-ethylthiophane, or thiepane, and cyclisation of the latter yields thiirane, which may dimerize to form 1,4-dithiane.

Mass spectra from Py–GC-MS

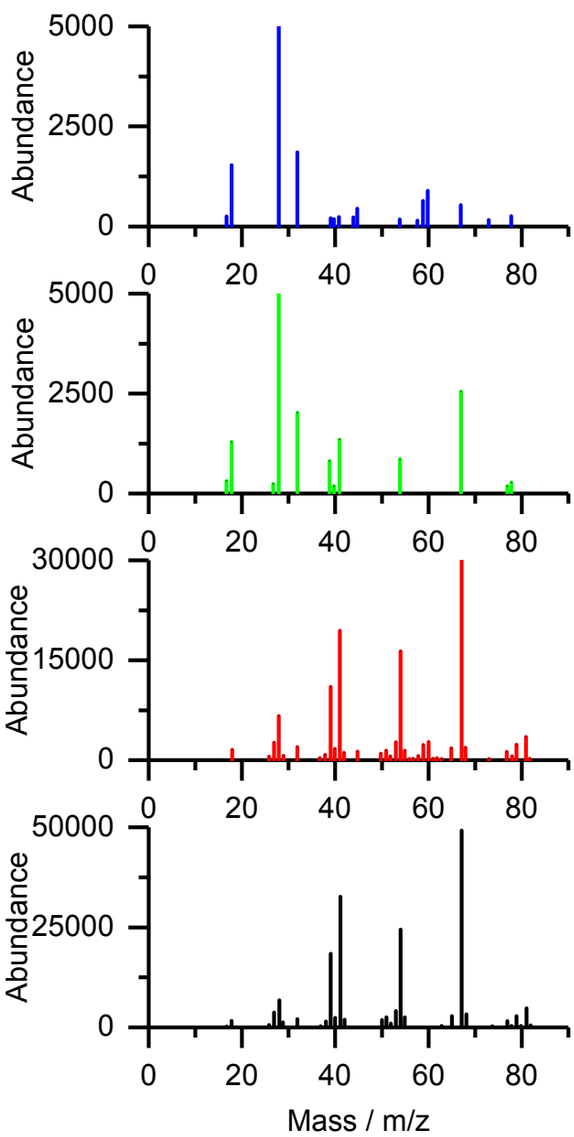

Figure S8. Mass spectra from Py-GC-MS measurements at a retention time of 2.6 min (blue region in Figure 4), assigned to 1,5-hexadiene.

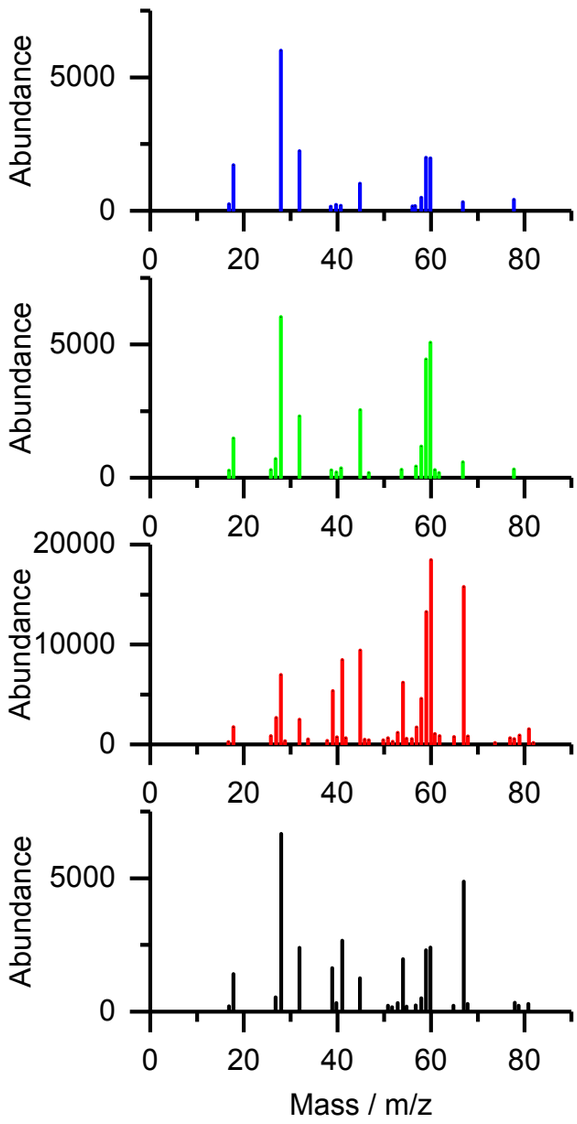

Figure S9. Mass spectra from Py-GC-MS measurements at a retention time of 2.63 min (yellow region in Figure 4), assigned to thiirane.

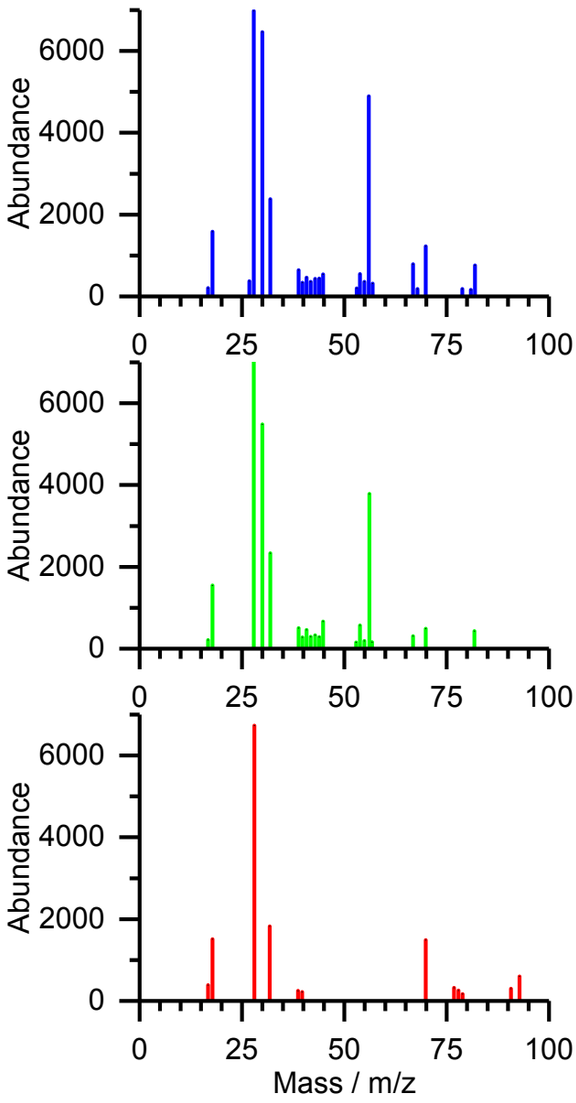

Figure S10. Mass spectra from Py-GC-MS measurements at a retention time of 6.1 min (purple region in Figure 4), assigned to 5-hexene-1-amine.

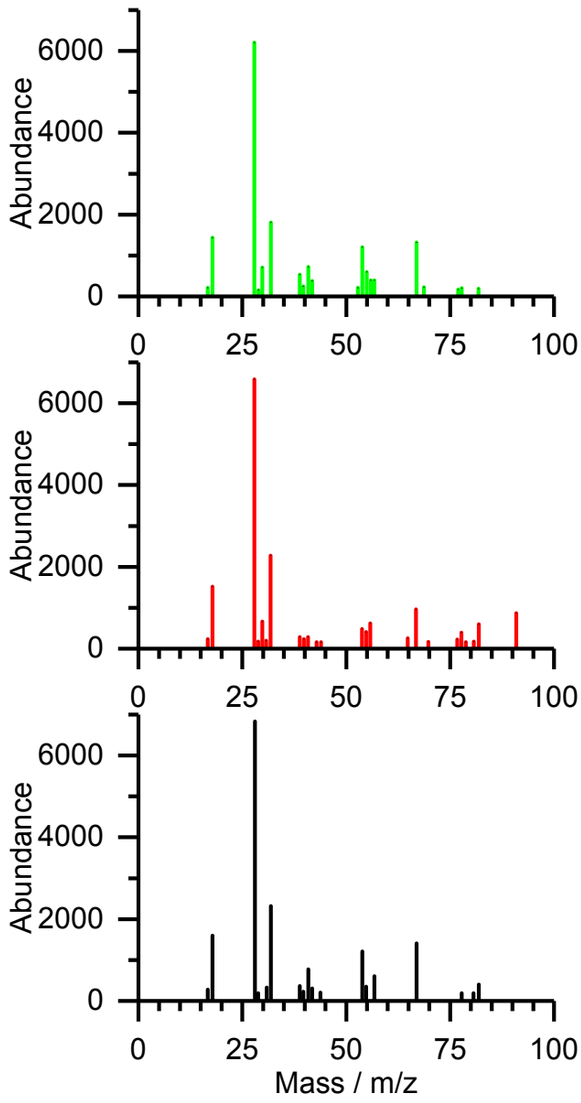

Figure S11. Mass spectra from Py-GC-MS measurements at a retention time of 6.6 min (purple region in Figure 4), assigned to 5-hexene-1-ol.

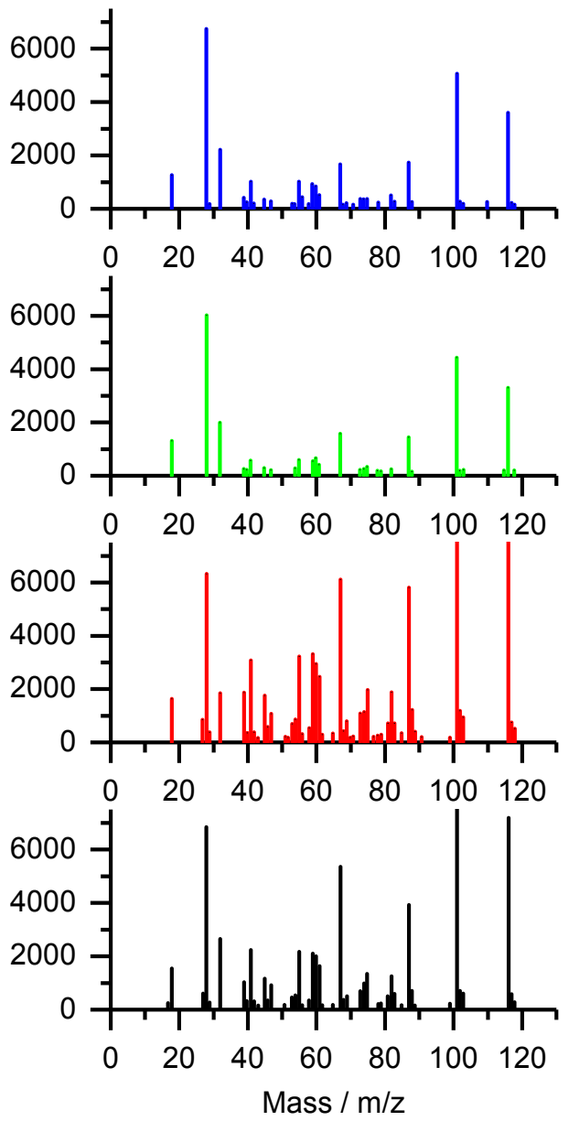

Figure S12. Mass spectra from Py-GC-MS measurements at a retention time of 7.8 min (yellow region in Figure 4), assigned to 4-methylthiane.

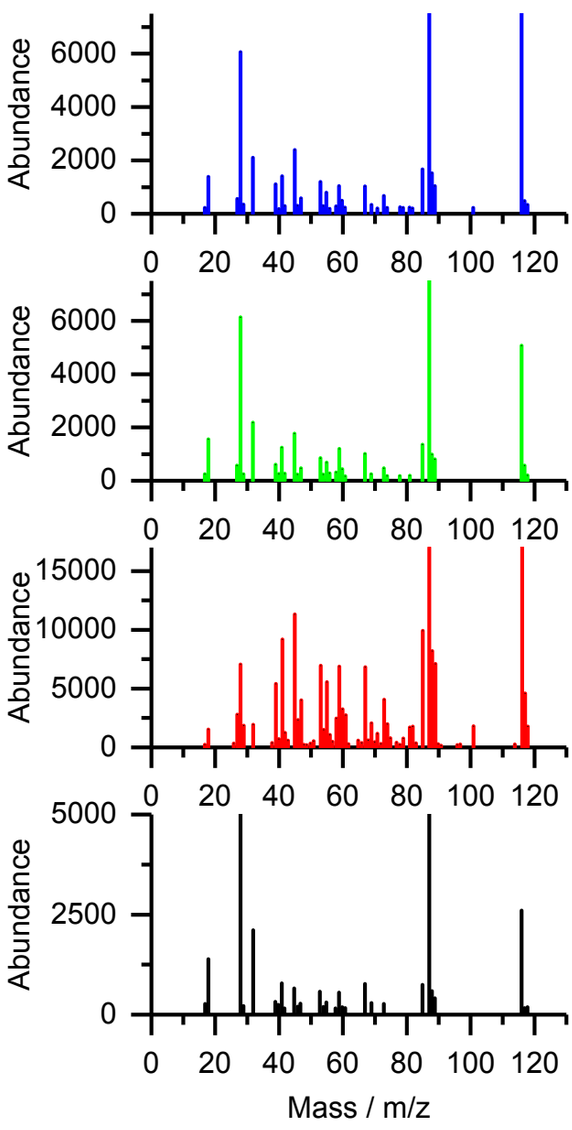

Figure S13. Mass spectra from Py-GC-MS measurements at a retention time of 8.2 min (yellow region in Figure 4), assigned to 2-ethylthiophane.

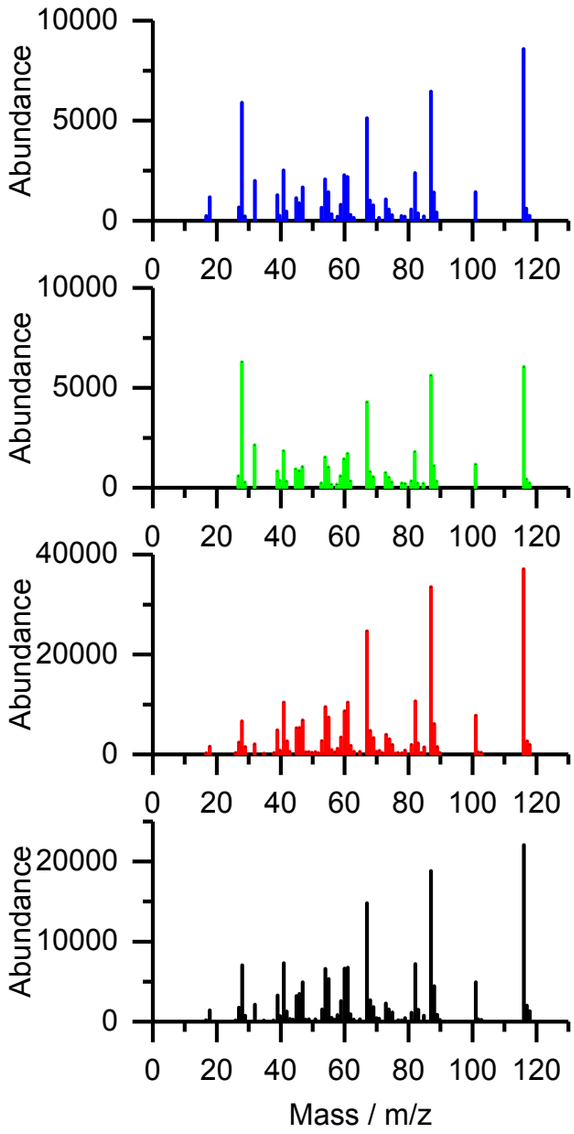

Figure S14. Mass spectra from Py-GC-MS measurements at a retention time of 9.3 min (yellow region in Figure 4), assigned to thiepane.

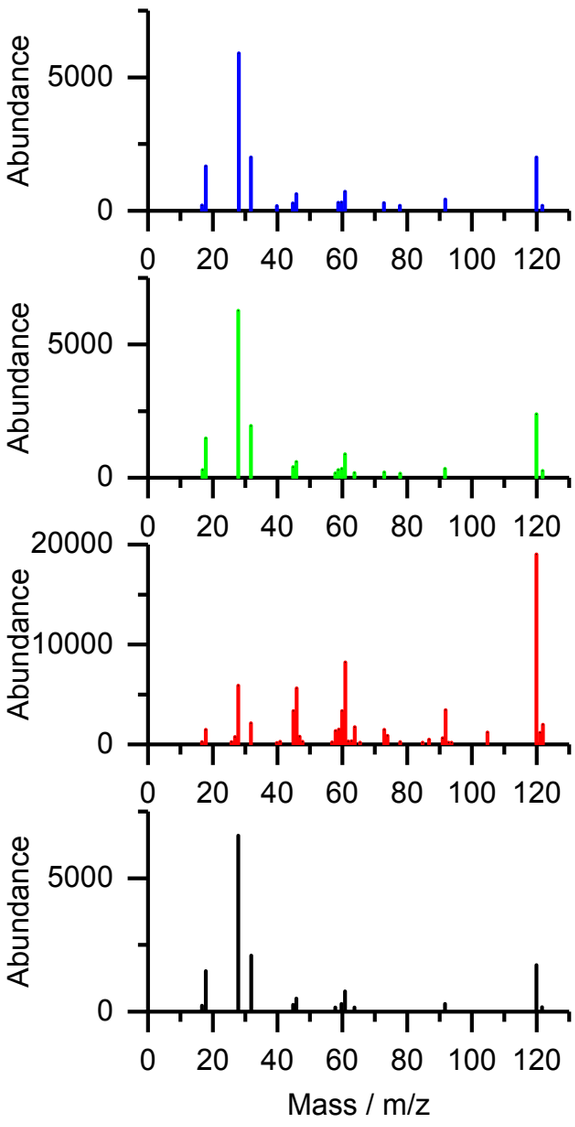

,

Figure S15. Mass spectra from Py-GC-MS measurements at a retention time of 10.2 min (yellow region in Figure 4), assigned to 1,4-dithiane.

Surface Etching

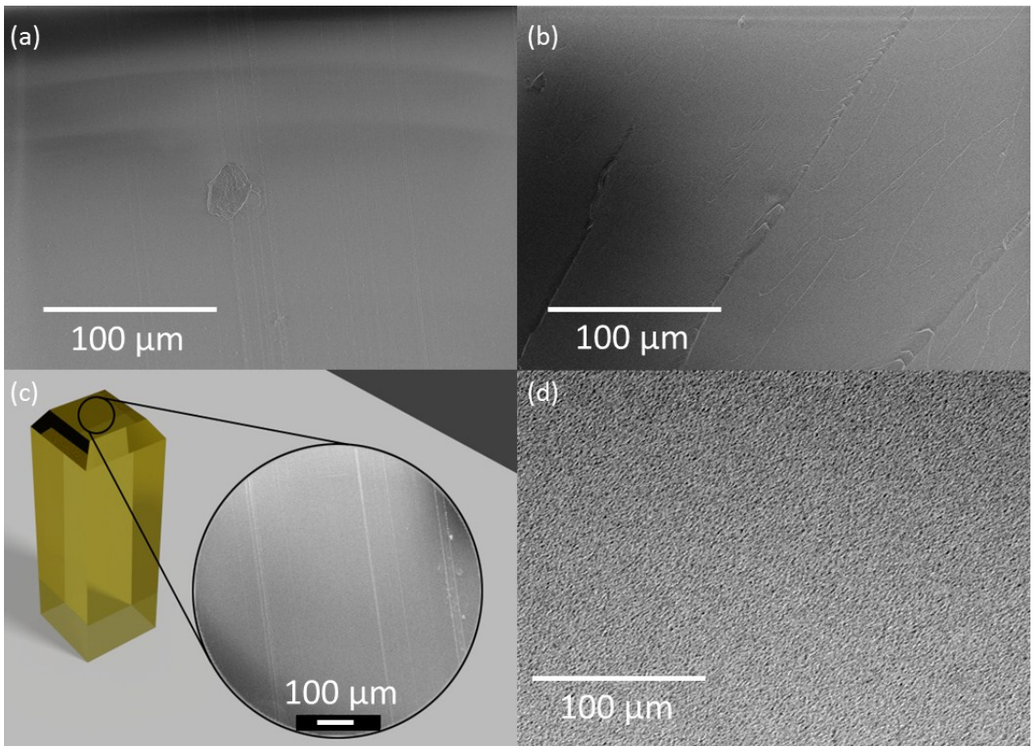

Figure S16. Electron microscopy images of EP-**4**: (a) SEM image of surface; (b) SEM image of surface after etching in dichloromethane under cryogenic conditions; (c) illustrated cut block used in etching experiments; (d) TEM image of surface stained with ruthenium tetroxide, showing no phase separation.

Glass-transition temperature from Differential Scanning Calorimetry

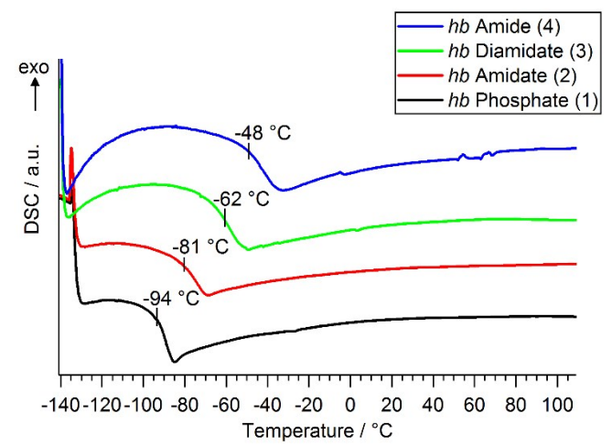

Figure S17. DSC curves of *hb*-FRs and noted glass-transition temperature (T_g)

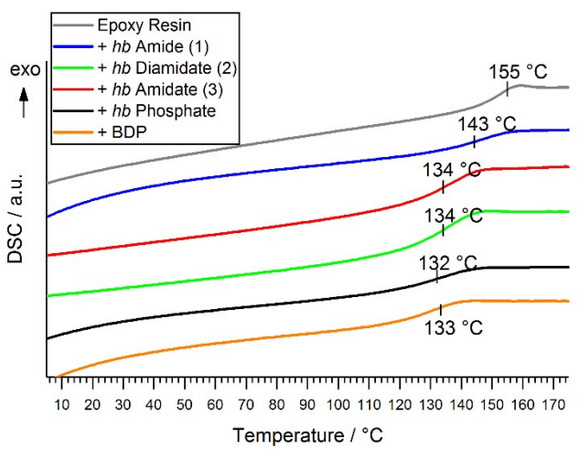

Figure S18. DSC curves of EP-*hb*-FRs and noted glass transition temperature (T_g).

Pyrolysis: Thermogravimetric Analysis of EP-*hb*-FRs

Table S4. Summary of TGA mass loss experiments of epoxy resins and flame retarded variants.

Material	$T_{5\%}$ / °C	T_{max} / °C	$T_{shoulder}$ / °C	*Mass loss / wt.-% (pre-main step)*	*Mass loss / wt.-% (main step)*	*Mass loss / wt.-% (shoulder)*	Residue / wt.-% (700 °C)
DGEBA-DMC	337.6 ± 0.9	372.4 ± 1.0	424.0 ± 5.0	-	62.0 ± 0.8	33.2 ± 0.3	4.5 ± 0.1
+ BDP	304.1 ± 1.2	357.3 ± 0.3	423.2 ± 0.1	-	74.6 ± 0.2	16.1 ± 0.3	8.2 ± 0.1
+ *hb* Phosphate (4)	288.6 ± 1.4	350.8 ± 1.2	423.8 ± 5.8	19.9 ± 0.1	54.6 ± 0.1	23.2 ± 0.7	7.7 ± 0.1
+ *hb* Amidate (3)	293.8 ± 3.2	351.8 ± 0.3	421.3 ± 3.9	-	77.8 ± 0.4	15.0 ± 0.2	6.8 ± 0.4
+ *hb* Diamidate (2)	286.6 ± 2.3	351.9 ± 2.0	423.2 ± 0.1	4.4 ± 0.2	69.8 ± 0.1	16.8 ± 0.2	8.1 ± 0.3
+ *hb* Amide (1)	282.6 ± 0.9	350.7 ± 1.2	420.5 ± 0.5	3.0 ± 0.1	74.7 ± 0.3	12.9 ± 0.2	8.0 ± 0.2

Pyrolysis: Condensed Phase Analysis

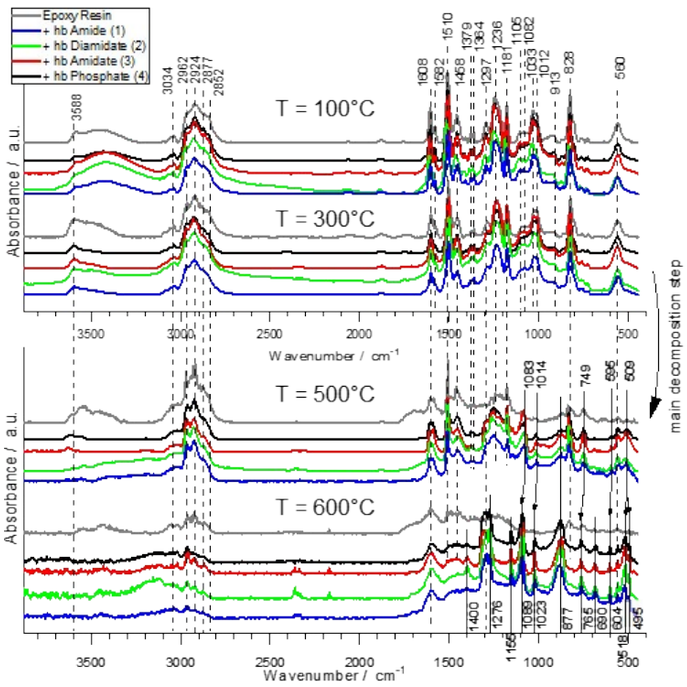

Figure S19. Condensed phase FTIR spectra of EP and EP-FRs at specific *T via* hot stage FTIR measurements. Dotted lines: EP signals; solid lines: P signals.

Table S5. Various phosphorus FTIR signals from literature compared to measured signals.

Measured [cm^{-1}]	Literature [cm^{-1}]	Group
2362	2200–2360[13]	R_2-(P=S)=O
	2600–2540[13]	R-(S-H)
1400	1100–1400 (cyclic compound)[14]	v(P=N)
	1230–1500 (acyclic compound)[14]	
1400	1380–1425[15]	(P-N-Ph)
1297–1276	1300–1250[15]	v(P=O);
1297–1276	1346–1255[13]	v_{sym}(P-CH_3)
1155	1240–1180[15]	R_2-(P=O)-OH
	1240–1190[15]	P-O-(Aryl-C)
1089	1130–1090[13]	v(P-Ph)
	1050–1030[15]	P-O-(Alkyl-C)
1023	1130–1090[15]	Phosphate (inorganic)
	1040–909[13]	v(P-OH)=O
877 (wide)	990–885[15]	P-O-P
	977–842 (interacts with P-O-C)[13]	δ_{wag}(P-H)
765, 690	754–634[13]	v(P-C)
604, 518, 495	540–485[14]	v_{skel}(C-C)

Hot Stage FTIR analysis was used to determine the changes in chemical structure of EP-*hb*-FRs in the condensed phase; spectra are from 100 °C, 300 °C (between $T_{5\%}$ and T_{max}), 500 °C (after T_{max}), and 600 °C (Figure S19). At $T > T_{max}$, i.e. the spectra at 500 and 600 °C, the disappearance of characteristic DGEBA-DMC bands of the EP was detected, due to thermal decomposition of the matrix as previously reported.[16] At T = 600 °C, there were only very few characteristic bands visible and the spectrum was very noisy due to complete decomposition. Especially bands at 1510 cm^{-1} (bisphenol A) and at 1224 and 1028 cm^{-1} (2-hydroxytrimethylene) showed a strong decrease in absorption due to volatilization of bisphenol A units. The EP-*hb*-FR spectra revealed the appearance of bands which were assigned to various phosphorus-containing species at T = 500 °C and especially at T = 600 °C (Table S5). Crucially, the band at 1400 cm^{-1} corresponding to (P=N) or (P-N-Ph) stretching vibrations and is visible for the resins with N-containing FRs, which correlates with previous investigations of the monomeric FR variants. This band was visible for EP-**4** as well, indicating that **4** interacts with the decomposing EP's amine component. The broad band between 1350–1250 cm^{-1} was assigned to the (P=O) or (P-CH_3) stretching vibration. The bands at 1155 cm^{-1} and the strong signal at 1089 cm^{-1} belong to (P=O) or aromatic hydrocarbons bound to phosphorus. The absorption band at 1089 cm^{-1} has also been noted in (-P-O-P-O) containing structures.[17] The broad band at 877 cm^{-1} was identified as those from di-substituted aromatic rings,[18, 19] but may also indicate the presence of (P-O-P) bonds.[20] The two bands at 765 and 690 cm^{-1} indicated the formation of (P-C) bonds.

Flammability: Reaction to Small Flames

EP and all EP-FRs were tested *via* UL-94 and limiting oxygen index (LOI) experiments to ascertain their flammability characteristics and reaction-to-small-flame behavior. The results of these experiments are summarized in Table S6. EP exhibited an oxygen index (OI) of 18.7 vol.-% in LOI experiments and the addition of FRs increased OI above 22 vol.-%. The benchmark FR BDP increased OI to the highest value of all tested materials (24.0 vol.-%). For *hb*-FRs, EP-**4** displayed the lowest OI of all tested materials (22.1 vol.-%), and the OI increased with increasing N-content in the P-binding sphere, with EP-**1** presenting the highest OI of all *hb*-FRs (23.3 vol.-%). Although the change in OI is not very pronounced, it is explained by the decomposition mechanism described in Scheme 2: *hb*-FRs with more (P-N) bonds form thermally stable char and suppress flammability more effectively than those materials with higher amounts of (P-O) bonds.

Table S6. Results of reaction-to-small-flame tests LOI and UL-94 for EP and EP-FRs.

	EP	EP-**1**	EP-**2**	EP-**3**	EP-**4**	EP-BDP
LOI						
O_2 / vol.-%	18.7 ± 0.3	23.3 ± 0.2	22.6 ± 0.2	22.5 ± 0.2	22.1 ± 0.2	24.0 ± 0.2
UL-94						
Classification	HB	HB	HB	HB75	HB	HB
Burn speed / mm s^{-1}	31.7 ± 3.6	22.0 ± 0.7	27.0 ± 0.1	41.8 ± 1.5	27.7 ± 4.4	19.6 ± 3.6

The UL-94 test results highlighted that all materials fail to attain a V-classification due mainly to the intense burning and the flaming dripping of the EP matrix. In horizontal tests, all materials achieved an HB classification, except EP-**3**. EP showed a burn speed of 31.7 mm s^{-1}, and EP-BDP attained the lowest burning speed at 19.6 mm s^{-1}. EP-*hb*-FRs exhibited lower burning speed than EP, and EP-**1** had the lowest value (22.0 mm s^{-1}). The reduction in burning speed in UL-94 tests also point to a reduction of flammability with increasing P-N bonds of the *hb*-system for the same reason. The reaction-to-small-flames experiments highlight that higher loadings than the chosen FR load (10 wt.-%) are necessary to attain OI-values and V-classification required for high-performance materials.[21] However, it must be stated that the results exemplify that a reduction of burning speed and a relative increase in OI of approx. 18–26% was possible already at relatively low loadings, signifying the efficacy of *hb*-FRs in EP.

Fire Behavior

Table S7. Maximum average rate of heat emission (MARHE) and fire growth rate (FIGRA) of EP and EP-FRs via cone calorimeter measurements.

	EP	EP-**1**	EP-**2**	EP-**3**	EP-**4**	EP-BDP
MARHE / kWm^{-2}	732 ±24	571 ±25	560 ±16	439 ±3	466 ±14	546 ±12
FIGRA / $kWm^{-2}\,s^{-1}$	15.5 ±2.3	10.0 ±0.1	8.1 ±0.1	7.5 ±0.6	9.0 ±0.2	11.0 ±0.7

The maximum average rate of heat emission (MARHE, from DIN CEN/TS 45545) and fire growth rate (FIGRA, from EN 13823) are used to assess fire protection behavior and help to quantify combustion and flame inhibition into tangible values (Table S7). For EP, the MARHE was 732 kW m^{-2} and the FIGRA was 15.5 kW m^{-2} s^{-1}. EP-BDP displayed a 25% lower MARHE (546 kW m^{-2}) and a 29% lower FIGRA (11.0 kW m^{-2} s^{-1}). Furthermore, all EP-*hb*-FRs exhibited a 22–36% reduction in MARHE and a 35–48% lower FIGRA. All *hb*-FRs reduced FIGRA more strongly than BDP, while only **3** and **4** lowered the MARHE more strongly than BDP. Although there are differences among the respective *hb*-FRs in terms of lowering PHRR, THE, MARHE, and FIGRA, the results speak for the ability of the chemical superstructure of the *hb*-FRs to perform on equal terms to an aromatic benchmark FR under forced flaming conditions, further illustrating their multifunctional abilities.

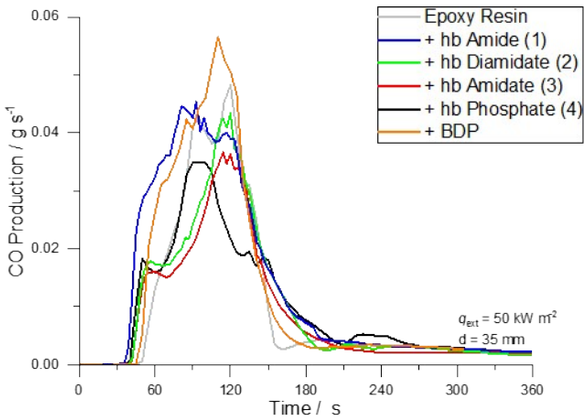

Figure S20. Carbon monoxide (CO) production over *t* of EP and EP-FRs during cone calorimeter measurements.

Table S8. CO yields (COY)

	EP	EP-**1**	EP-**2**	EP-**3**	EP-**4**	EP-BDP
COY / 10^{-2} g g^{-1}	9.0 ±1.0	12.9 ±0.5	9.8 ±0.2	9.4 ±0.1	9.9 ±0.1	11.3 ±0.7

Figure S20 shows the carbon monoxide (CO) production during cone calorimeter measurements, and CO yields (COY) are displayed in Table S8. The CO production during combustion is crucial to understanding the FR effect: a reduction in χ (combustion efficiency) is accompanied by an increase in CO and smoke production, as they are byproducts of an incomplete combustion. Consequently, efficient flame inhibition is intrinsically accompanied by an increase in COY.[22] EP showed a CO yield of 9.0 · 10^{-2} g g^{-1}, while EP-BDP exhibited a 26% increase in COY. The *hb*-FRs increased COY by 4–43%: EP-**1** showed the largest COY increase (43%), indicating the most incomplete combustion for this material, while EP-**3** displayed the lowest relative COY increase at 4%. Table 1 also compares the material's EHC, which is a parameter for gas phase activity, and a reduction in EHC signifies effective flame inhibition.[23] BDP, **3**, and **4** lowered EHC in EP by 16, 6 and 10%, respectively, while **2** had no effect on EHC of EP, and **1** actually increased EHC by 5%. These results provide further evidence that *hb*-FRs with higher O-content in the binding sphere of P show a stronger gas phase mechanism resulting in lower EHC, while those with higher N-content present a more pronounced condensed phase mechanism that leads to a decreased combustion efficiency and higher CO yield. These findings correlate well with the mass loss behavior of *hb*-FRs under pyrolysis, where a critical O:N ratio governed the decomposition behavior.

Residue analysis:

The residues from cone calorimeter tests were investigated *via* scanning electron microscopy (SEM) and elemental analysis to understand the micro- and macroscopic effects of *hb*-FRs on EP. The residues in Figure S21 exemplify the condensed phase effect of *hb*-FRs: Figure S21a shows an EP specimen before and Figure S21b displays the residue after cone calorimeter measurements. EP combusted almost completely with only a very small residue amount (0.7 wt.-%). For EP-*hb*-FRs (Figure S21d,e,h,i), the formation of char fixed fuel into the condensed phase leading to increased residue yields (7–12 wt.-%). The residues had a puffy, foam-like structure. The voluminous structure pointed to an intumescent system, as evidenced by the swollen characteristic of the char-structure averaging at 4 cm in height (Figure S21e,i). Cross-sections of the residues revealed a multicellular structures, and SEM images from the residue surfaces (Figure S21f,j) and cores (Figure S21g,k) provided further evidence of an intumescent system.[24, 25] The morphology of the residue cores consisted of a 3-D network of bubble-like surfaces with an open cell structure.[26] The bubbles' diameter ranged from <300 µm for EP-**1** to roughly 500 µm for EP-**4**. The surface images exemplify that the protective layer of the intumescent char relied on the formation of bubbles insulating the underlying material from irradiation. The bubbles near the top of the sample were exposed to radiation and thermo-oxidation after flame-out, leading to a fusing of the cells and the formation of a rough carbonaceous surface topography. This explains the phenomenon seen in cone calorimeter measurements, where a decline in HRR and a small plateau-like shape of the HRR(*t*) curve roughly 20–30 s after the ignition was observed. The decomposing material formed an intumescent foam and when the top layer decomposed, its insulating properties diminished, resulting in renewed decomposition of the underlying material. Notably, the bubble-size for EP-**4** were larger than those in EP-**1**. This phenomenon results from increased partial pressure inside the material caused by the higher gas production of EP-**4** during decomposition, which led to better thermal insulation and lower PHRR.

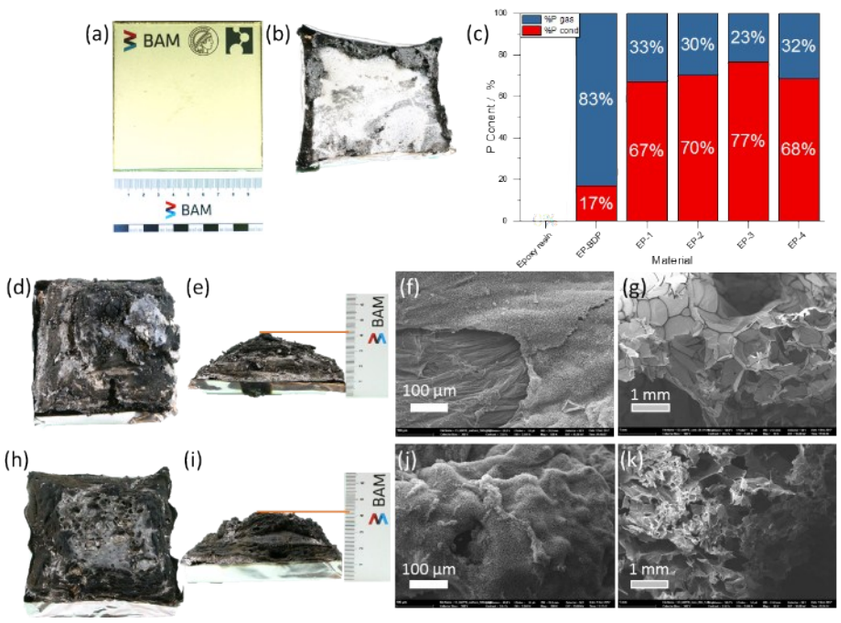

Figure S21. Residue analysis of samples after cone calorimeter experiments; (a) Image of EP specimen before measurement; (b) EP specimen after measurement, exhibiting little residue; (c) P-content in gas (blue) and condensed (red) phase, calculated *via* elemental analysis of residues; (d,h) Residue image (top view) of EP-**4** and EP-**1**; (e,i) Residue image (profile view) of EP-4 and EP-1; (f,j) SEM images of EP-**4** and EP-**1** residue surface; (g,k) SEM image of EP-**4** and EP-**1** residue core.

Figure S21c portrays the P-content in the condensed phase (red) of residues after cone calorimeter measurements *via* elemental analysis. The amount of P present in the gas phase (blue) was calculated by subtracting the measured mass of P in the residue from the calculated mass of P in the initial EP-FR. As Figure S21c shows, BDP had 17% P-content in the condensed phase, meaning 83% of P went into the gas phase, which is in accordance with previous findings.[8, 27] Figure S21c also displays that, while there are differences in the P-content among them, all *hb*-FRs exhibited between 67–77% P-content in the condensed and 23–33% in the gas-phase. This corresponds well with the increase in residue yields of EP-*hb*-FRs in forced-flaming tests and showcases the ability of *hb*-FRs to retain fuel *via* specific reactions of P in the condensed phase. It should be noted that the elemental analysis was performed on residue samples

taken after cone calorimeter measurements (end of test) and not specifically at flame-out, meaning there is substantial thermo-oxidation of the sample. As many (P-N)-containing species are not thermally stable, their decomposition during thermo-oxidation explains the lower P-content of EP-**1** and EP-**2** samples.

However, when comparing *hb*-FRs to their low molar mass monomers, the results from elemental analysis point to a shift in mode of action. In previous findings, the monomer of **1** exhibited an 80% P-content in the condensed phase, while the monomer of **2** displayed 55% P-content in the gas phase.[28] This change in condensed phase activity can be rationalized by the increase in chemical interaction between EP and FR during combustion due to the higher thermal stability of *hb*-FR, further highlighting the multifunctional capabilities of P-FRs with complex molecular architectures.

References

1. D. Marsh, *The Kinetics of the Thermal Decomposition of Isopropyl Methylphosphonofluoridate*, Chemical Defence Experimental Establishment Porton Down (United Kingdom), 1954.
2. K. N. Bauer, L. Liu, D. Andrienko, M. Wagner, E. K. Macdonald, M. P. Shaver and F. R. Wurm, *Macromolecules*, 2018, **51**, 1272-1279.
3. P. A. Glaude, C. Melius, W. J. Pitz and C. K. Westbrook, *P Combust Inst*, 2002, **29**, 2469-2476.
4. S. Hörold, *Polymer Degradation and Stability*, 1999, **64**, 427-431.
5. W. Gerrard, *J Chem Soc*, 1944, DOI: DOI 10.1039/jr9440000085, 85-90.
6. R. W. Baier and S. W. Weller, *Ind Eng Chem Proc Dd*, 1967, **6**, 380-&.
7. S. Gaan, G. Sun, K. Hutches and M. H. Engelhard, *Polymer Degradation and Stability*, 2008, **93**, 99-108.
8. S. V. Levchik and E. D. Weil, *Journal of Fire Sciences*, 2006, **24**, 345-364.
9. S. V. Levchik, G. F. Levchik, A. I. Balabanovich, E. D. Weil and M. Klatt, *Angew Makromol Chem*, 1999, **264**, 48-55.
10. C. Nguyen and J. Kim, *Polymer Degradation and Stability*, 2008, **93**, 1037-1043.
11. S. V. Levchik, in *Flame Retardant Polymer Nanocomposites*, eds. A. B. Morgan and C. A. Wilkie, John Wiley & Sons, Inc., 2006, DOI: 10.1002/9780470109038.ch1, pp. 1-29.
12. E. D. Weil, *Fire retardancy of polymeric materials*, 2000, 115-145.
13. C. Hampton, D. Demoin and R. E. J. O. S. Glaser, 2010.
14. G. Socrates, *Infrared and Raman characteristic group frequencies: tables and charts*, John Wiley & Sons, 2004.
15. M. Hesse, H. Meier and B. Zeeh, *Spektroskopische Methoden in der organischen Chemie*, Georg Thieme Verlag, 2005.
16. B. Perret, B. Schartel, K. Stöß, M. Ciesielski, J. Diederichs, M. Döring, J. Krämer and V. Altstädt, *European Polymer Journal*, 2011, **47**, 1081-1089.
17. L. C. Thomas, *Interpretation of the infrared spectra of organophosphorus compounds*, Heyden London, 1974.
18. A. S. Politou, C. Morterra and M. J. D. Low, *Carbon*, 1990, **28**, 529-538.
19. M. C. Despinasse and B. Schartel, *Thermochimica Acta*, 2013, **563**, 51-61.
20. U. Braun, A. I. Balabanovich, B. Schartel, U. Knoll, J. Artner, M. Ciesielski, M. Döring, R. Perez, J. K. W. Sandler, V. Altstädt, T. Hoffmann and D. Pospiech, *Polymer*, 2006, **47**, 8495-8508.
21. A. F. Grand and C. A. Wilkie, *Fire retardancy of polymeric materials*, CRC Press, 2000.
22. B. Schartel, *Materials*, 2010, **3**, 4710-4745.
23. B. Schartel, B. Perret, B. Dittrich, M. Ciesielski, J. Krämer, P. Müller, V. Altstädt, L. Zang and M. Döring, *Macromolecular Materials and Engineering*, 2016, **301**, 9-35.
24. J. Alongi, Z. D. Han and S. Bourbigot, *Progress in Polymer Science*, 2015, **51**, 28-73.
25. P. Müller, M. Morys, A. Sut, C. Jäger, B. Illerhaus and B. Schartel, *Polymer Degradation and Stability*, 2016, **130**, 307-319.
26. S. Bourbigot and M. Le Bras, in *Plastics Flammability Handbook*, ed. J. Troitzsch, Carl Hanser Verlag GmbH & Co. KG, Munich, 2004, DOI: 10.3139/9783446436695.005, pp. 133-172.
27. S. Rabe, Y. Chuenban and B. Schartel, *Materials*, 2017, **10**, 23.
28. J. C. Markwart, A. Battig, L. Zimmermann, M. Wagner, J. Fischer, B. Schartel and F. R. Wurm, *ACS Applied Polymer Materials*, 2019, **1**, 1118-1128.